

SOURCE LOCALIZATION USING AIRBORNE VECTOR SENSORS

Hasan S. Mir and John D. Sahr

University of Washington, Seattle
{hmir, jdsahr}@ee.washington.edu

Catherine M. Keller

MIT Lincoln Laboratory
keller@ll.mit.edu

ABSTRACT

The direction finding (DF) performance of an array of vector sensor antennas on a small aircraft is assessed. DF performance in the presence of additive noise, array manifold perturbations, and uncertainty of polarization parameters is examined with simulated data and compared to the Cramer-Rao lower bound. DF performance improvements are demonstrated with a least-squares type calibration technique with and without the use of synthetic antenna elements.

1. INTRODUCTION

A key application of sensor arrays is the passive localization of a radiating signal source. The sensor-to-sensor delays contain information about the source location in terms of the source azimuth angle θ and source elevation angle ϕ for two dimensional array configurations. This information is exploited in direction finding (DF) algorithms that estimate the source angle-of-arrival (AOA). DF algorithms utilize an underlying model which presumes a coherent phase relationship among the antenna array elements. Such a relationship almost never occurs in practice due to various antenna effects such as antenna pattern differences and antenna-to-receiver electrical cable length differences. Thus, array calibration, which attempts to fit the actual array response to the theoretical response, is essential for obtaining accurate DF estimates.

The angular resolution of an array is directly related to the size of its aperture. For airborne applications in which a sensor array is mounted on a small aircraft, the physical space available on the airframe is limited and the array aperture is restricted. Earlier work in [1] proposed the use of a single vector sensor consisting of two orthogonal triads of dipole and loop antennas with the same phase center for

This work was sponsored by the Department of Defense under Air Force Contract F19628-00-C-0002. Opinions, interpretations, conclusions, and recommendations are those of the authors and are not necessarily endorsed by the United States Government.

The authors acknowledge the work of Dan Bliss, Amanda Chan, and Alex Eapen for their modeling work to establish an appropriate vector sensor array for a small aircraft.

source localization. Because a vector sensor uses multiple components of electromagnetic information, it can offer accurate AOA estimates with a smaller aperture.

This paper examines the problem of using vector sensors mounted on a small aircraft to perform source localization. Section 2 contains background material and formulates the signal model. Section 3 presents and discusses the simulation results. Section 4 provides the conclusion.

2. PROBLEM FORMULATION

Initial work with a vector sensor mounted on an aircraft has indicated that some elements of the vector sensor act as “feeds” for the airframe, rendering them unusable. The proposed solution is to use a “trimmed” vector sensor employing only the elements with insignificant airframe interaction. Multiple trimmed vectors sensors are sited at various locations on the airframe so that additional sensor elements are available for accurate AOA estimates.

An example of a trimmed vector sensor is shown in Fig. 1(a). The two loop antennas measure the x and y components of the magnetic field, while the vertical dipole measures the z component of the electric field. Fig. 1(b) shows a potential 8-channel configuration for placement on an aircraft that will be studied in this paper. The trimmed vector sensors on the aircraft are not all identical; the one mounted on the nose of the airframe lacks the vertical dipole.

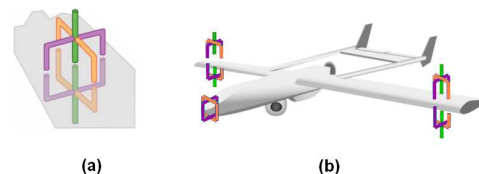


Fig. 1. (a) Trimmed vector sensor consisting of two loop and one dipole antenna. (b) 8-channel aircraft configuration.

2.1. Signal Model

It is assumed (as in e.g. [1]) that the vector sensor array is in the far-field of a narrowband signal. Following [2], define

the components of the electric and magnetic field received on the array as

$$\begin{bmatrix} E_x \\ E_y \\ E_z \\ H_x \\ H_y \\ H_z \end{bmatrix} = \begin{bmatrix} \cos(\theta) \cos(\phi) & -\sin(\theta) \\ \sin(\theta) \cos(\phi) & \cos(\theta) \\ -\sin(\phi) & 0 \\ -\sin(\theta) & -\cos(\theta) \cos(\phi) \\ \cos(\theta) & -\sin(\theta) \cos(\phi) \\ 0 & \sin(\phi) \end{bmatrix} \begin{bmatrix} \sin(\gamma) e^{+j\eta} \\ \cos(\gamma) \end{bmatrix} \quad (1)$$

where $\Theta(\theta, \phi)$ and $\mathbf{p}(\gamma, \eta)$ are defined appropriately, and $0^\circ \leq \gamma \leq 180^\circ$ and $-180^\circ \leq \eta \leq 180^\circ$ are the polarization angle and phase difference, respectively. Let \mathbf{r}_k be a matrix of sensor locations and $\Theta_k(\theta, \phi)$ be the appropriate row of $\Theta(\theta, \phi)$ corresponding to the particular field component being measured. Define a unit vector in the source direction

$$\mathbf{u}(\theta, \phi) = [\cos(\theta) \sin(\phi) \quad \sin(\theta) \sin(\phi) \quad \cos(\phi)]^T$$

where the superscript T denotes transpose. The plane wave (far-field) response is defined as

$$\mathbf{q}_k(\theta, \phi) = e^{+j \frac{2\pi}{\lambda} \mathbf{r}_k^T \mathbf{u}(\theta, \phi)} \quad (2)$$

where λ is the signal wavelength. The response of the vector sensor array is

$$\mathbf{v}(\theta, \phi, \gamma, \eta) = [\mathbf{v}_1(\theta, \phi, \gamma, \eta)^T \quad \dots \quad \mathbf{v}_K(\theta, \phi, \gamma, \eta)^T]^T \quad (3)$$

where

$$\mathbf{v}_k(\theta, \phi, \gamma, \eta) = \mathbf{q}_k(\theta, \phi) [\Theta_k(\theta, \phi) \mathbf{p}(\gamma, \eta)] \quad (4)$$

and K is the number of distinct measured fields.

For the trimmed vector sensor measuring the three components H_x , H_y , and E_z , $K = 3$. Letting q_{lw} , q_{rw} , and q_t represent the plane wave response for the vector sensor on the left wing, right wing, and tip of the aircraft, respectively,

$$\mathbf{v}(\theta, \phi, \gamma, \eta) = \begin{bmatrix} E_z \begin{pmatrix} q_{lw} \\ q_{rw} \end{pmatrix} \\ H_x \begin{pmatrix} q_{lw} \\ q_{rw} \\ q_t \end{pmatrix} \\ H_y \begin{pmatrix} q_{lw} \\ q_{rw} \\ q_t \end{pmatrix} \end{bmatrix}$$

is an 8×1 response vector.

For an additive noise scenario, the received signal is expressed as

$$\mathbf{x}(t) = \mathbf{v}(\theta, \phi, \gamma, \eta) s(t) + \mathbf{n}(t) \quad (5)$$

where $s(t)$ is the transmitted signal with power σ_s^2 and $\mathbf{n}(t)$ is the additive noise with variance σ_w^2 .

2.2. Model Perturbations and Calibration

In practice, additive noise as well as perturbations to the sensor manifold are present. Many DF algorithms such as MuSIC and MVDR/Capon utilize a search procedure that assumes knowledge of the actual manifold. Using only the theoretical array manifold can lead to misleading results. To compensate for sensor anomalies, external calibration is performed by attempting to fit the measured response to a modeled response.

With known source AOAs, the benchmark external calibration algorithm PRESS (Pattern Response Equalization Via Spatial Similarity) [3] can be used. Suppose an M channel sensor array observes a stationary, far-field, narrowband source at L distinct angles. Let $\mathbf{v}(\theta_l, \phi_l)$ and $\mathbf{z}(\theta_l, \phi_l)$ represent the $M \times 1$ modelled and measured sensor response vector, respectively, for the source elevation AOA θ_l and azimuth AOA ϕ_l , where $l = 1 \dots L$. Define the $M \times L$ matrices

$$\mathbf{V}(\boldsymbol{\theta}_T, \boldsymbol{\phi}_T) = [\mathbf{v}(\theta_1, \phi_1) \quad \dots \quad \mathbf{v}(\theta_L, \phi_L)] \\ \mathbf{Z}(\boldsymbol{\theta}_T, \boldsymbol{\phi}_T) = [\mathbf{z}(\theta_1, \phi_1) \quad \dots \quad \mathbf{z}(\theta_L, \phi_L)]$$

where $\boldsymbol{\theta}_T$ and $\boldsymbol{\phi}_T$ are vectors whose l th element is θ_l and ϕ_l , respectively. The PRESS algorithm computes a calibration matrix $\mathbf{A} \in \mathbb{C}^{M \times M}$ using the least-squares criterion

$$\arg \min_{\mathbf{A}} \sum_{l=1}^L \|\mathbf{z}(\theta_l, \phi_l) - \mathbf{A} \mathbf{v}(\theta_l, \phi_l)\|^2 \quad (6) \\ = \arg \min_{\mathbf{A}} \|\mathbf{Z}(\boldsymbol{\theta}_T, \boldsymbol{\phi}_T) - \mathbf{A} \mathbf{V}(\boldsymbol{\theta}_T, \boldsymbol{\phi}_T)\|_F^2$$

where the subscript F denotes the Frobenius norm. This yields

$$\mathbf{A} = \mathbf{Z}(\boldsymbol{\theta}_T, \boldsymbol{\phi}_T) \mathbf{V}^\#(\boldsymbol{\theta}_T, \boldsymbol{\phi}_T) \quad (7)$$

as the optimum solution for the PRESS calibration matrix, where $\#$ denotes the Moore-Penrose pseudoinverse. The PRESS calibration matrix reduces the distance between the measured and modelled steering vector, and is therefore useful in source localization applications.

It is possible to further improve source localization accuracy by augmenting the PRESS algorithm with synthetic elements. Selection of the placement and polarization of the synthetic elements is an open problem. In this paper, an ad-hoc placement for synthetic elements is chosen as the sensors missing from the trimmed vector sensors. For example, because a full vector sensor consists of 6 elements, the 8-channel configuration of Fig. 1(b), which consists of 3 distinct sub-arrays, would have a modelled response vector of length 18 when synthetic elements are used.

3. SIMULATION RESULTS

For simulation studies, the aircraft geometry at 90 MHz is shown in Fig. 2. Sensor manifold perturbations are assumed to be caused by near-field scatterers local to the airframe. This is modeled using the equation

$$\mathbf{z}(\theta, \phi) = \mathbf{v}(\theta, \phi) + \varepsilon \sum_{n=1}^{N_{scat}} \mathbf{q}(\theta_n, \phi_n) [\Theta(\theta_n, \phi_n) \mathbf{\Gamma}_n \mathbf{p}(\gamma, \eta)] e^{+j d_n} \quad (8)$$

where $\mathbf{\Gamma}_n$ is a 2×2 random scattering matrix and d_n is the path length difference. The parameter ε determines the relative strength of the multipath component and N_{scat} is the number of scatterers. For the simulations, $\varepsilon = 10$ dB and $N_{scat} = 20$.

AOA estimation is performed using the Capon MVDR estimator

$$\arg \min_{\theta, \phi} \frac{1}{(\mathbf{A} \mathbf{v}(\theta, \phi))^H \mathbf{R}_x^{-1} (\mathbf{A} \mathbf{v}(\theta, \phi))} \quad (9)$$

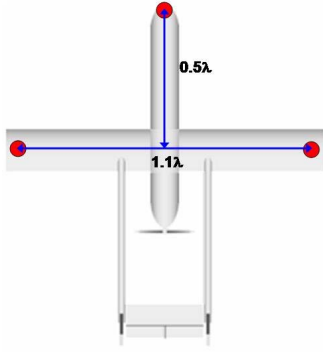


Fig. 2. Small aircraft geometry at 90 MHz

where the superscript H denotes conjugate transpose (Hermitian), and \mathbf{R}_x is the autocorrelation matrix of the received signal (5). If no calibration is used, then $\mathbf{A} = \mathbf{I}$. Source localization performance is assessed using the root mean square error (RMSE) criterion. The RMSE is compared against the Cramer-Rao lower bound (CRLB), which is derived in the Appendix.

Sensor manifold perturbations are introduced to the modeled response vectors within a 90° sector in azimuth and a 30° sector in elevation. Source localization performance is assessed for the following scenarios:

1. **Noise only:** It is assumed that noise is the only impairment, and exact knowledge of the sensor manifold is available to perform AOA estimation.
2. **No calibration:** It is assumed that both noise and sensor manifold perturbations are present. The modeled steering vectors are used to perform AOA estimation.
3. **PRESS:** This is the same as the Scenario 2, except that the modeled steering vector is premultiplied by the PRESS calibration matrix (computed as described in Section 2.2) when used to perform AOA estimation.
4. **Synthetic:** This is the same as Scenario 3, except that synthetic elements are included to compute the PRESS matrix and modeled steering vectors.

In Figure 3, AOA estimate errors are averaged over the azimuth and elevation sectors described above. The calibration residual for Scenarios 2 through 4, defined as

$$C = 10 \log_{10} \left[\frac{\sum_l \|\mathbf{z}(\theta_l, \phi_l) - \mathbf{A}\mathbf{v}(\theta_l, \phi_l)\|^2}{\sum_l \|\mathbf{z}(\theta_l, \phi_l)\|^2} \right] \text{ dB} \quad (10)$$

is 0.3 dB with no calibration, -25.8 dB after PRESS calibration, and -45.4 dB after PRESS calibration using synthetic elements. Fig. 3 (a) and (b) show the source localization RMSE dependence on the array signal-to-noise ratio

(ASNR), defined as $\text{ASNR} = N_{\text{channels}} \sigma_s^2 / \sigma_w^2$, where for this simulation $N_{\text{channels}} = 8$. The polarization parameters have value $\gamma = 50^\circ$ and $\eta = 60^\circ$, which are assumed to be known. In Fig. 3, it can be seen that the use of PRESS calibration offers significant reductions in azimuth and elevation angle RMSE from those of the no calibration scenario. For high SNR, the use of synthetic elements reduces the RMSE from that of PRESS alone. For the noise only scenario, an exact characterization of the array manifold is available, and the RMSE continues to approach the CRLB as ASNR increases. However, for Scenarios 2 through 4, the RMSE reaches a plateau for high ASNR because exact calibration is not possible.

Fig. 3(a) and (b) assume perfect knowledge of the polarization parameters. In Fig. 3(c) and (d), the effects of perturbing the polarization parameters is examined while holding the ASNR constant at 10 dB. For simplicity, the parameters γ and η are perturbed by the same amount. It is observed that the RMSE behavior is approximately symmetric about 0° perturbations.

Fig. 4 and 5 are an example of the Capon estimator spectrum for the scenarios enumerated earlier in this section. That the use of PRESS or synthetic elements significantly helps in reducing the width of the peak, as compared to the no calibration scenario which has a very spread out peak, is obviated in Fig. 4. Fig. 5 shows the spherical coordinate plot of the surfaces contoured in Fig. 4. The line in Fig. 5 points in the true source direction. It is to be noted again that the use of PRESS and synthetic elements significantly helps in localizing the beam around the true source direction.

In general, the beam pattern will change according to the incident polarization, and thus some variation in Fig. 3-5 can be expected as well. The investigation of the dependence of performance on all different polarization states, however, is deferred to the future.

4. CONCLUSION

Vector sensors are useful in applications where limited available physical space necessitates sensor arrays with reduced aperture. The source localization performance of multiple trimmed vector sensors for a geometric configuration applicable to a small aircraft was assessed. Source-localization performance in the presence of additive noise, sensor manifold perturbations, and uncertainty of polarization parameters was assessed. It was shown that significant performance gains can be achieved with the use of PRESS calibration and PRESS calibration incorporating synthetic elements.

5. APPENDIX: DERIVATION OF THE CRAMER-RAO LOWER BOUND

Define the real parameter vector $\boldsymbol{\psi} = [\theta \ \phi \ \gamma \ \eta]^T$. The received signal becomes

$$\mathbf{x}(t) = \mathbf{v}(\boldsymbol{\psi}) s(t) + \mathbf{n}(t). \quad (11)$$

The autocorrelation of the received signal is

$$\begin{aligned} \mathbf{R}_x &= E \{ \mathbf{x} \mathbf{x}^H \} \\ &= \sigma_s^2 \mathbf{v}(\boldsymbol{\psi}) \mathbf{v}^H(\boldsymbol{\psi}) + \sigma_w^2 \mathbf{I}. \end{aligned} \quad (12)$$

Assuming that $n(t)$ is a zero-mean Gaussian process uncorrelated with the signal, the Fisher Information Matrix for B snapshots is given by

$$[\mathbf{J}_{\boldsymbol{\psi}\boldsymbol{\psi}}]_{ij} = B \text{ trace} \left\{ \mathbf{R}_x^{-1} \frac{\partial \mathbf{R}_x}{\partial \psi_i} \mathbf{R}_x^{-1} \frac{\partial \mathbf{R}_x}{\partial \psi_j} \right\}. \quad (13)$$

The Cramer-Rao lower bound (CRLB) is thus

$$\text{CRLB}(\theta, \phi) = \left[\mathbf{J}_{(\theta, \phi)(\theta, \phi)} - \mathbf{J}_{(\theta, \phi)(\gamma, \eta)} \mathbf{J}_{(\gamma, \eta)(\gamma, \eta)}^{-1} \mathbf{J}_{(\gamma, \eta)(\theta, \phi)} \right]^{-1}. \quad (14)$$

The relevant derivatives are computed below.

$$\begin{aligned} \frac{\partial \mathbf{R}_x}{\partial \psi_i} &= \sigma_s^2 \frac{\partial \mathbf{v}(\boldsymbol{\psi})}{\partial \psi_i} \mathbf{v}^H(\boldsymbol{\psi}) + \sigma_s^2 \mathbf{v}(\boldsymbol{\psi}) \frac{\partial \mathbf{v}^H(\boldsymbol{\psi})}{\partial \psi_i} \\ \frac{\partial \mathbf{v}_k(\boldsymbol{\psi})}{\partial (\theta, \phi)} &= \left[\frac{\partial \mathbf{q}_k(\theta, \phi)}{\partial (\theta, \phi)} \Theta_k(\theta, \phi) + \mathbf{q}_k(\theta, \phi) \frac{\partial \Theta_k(\theta, \phi)}{\partial (\theta, \phi)} \right] \mathbf{p}(\gamma, \eta) \\ \frac{\partial \mathbf{q}_k(\theta, \phi)}{\partial (\theta, \phi)} &= j \frac{2\pi}{\lambda} \text{diag} \left\{ \mathbf{r}_k^T \frac{\partial \mathbf{u}(\theta, \phi)}{\partial (\theta, \phi)} \right\} \mathbf{q}_k(\theta, \phi) \\ \frac{\partial \mathbf{v}_k(\boldsymbol{\psi})}{\partial (\gamma, \eta)} &= [\mathbf{q}_k(\theta, \phi) \Theta_k(\theta, \phi)] \frac{\partial \mathbf{p}(\gamma, \eta)}{\partial (\gamma, \eta)} \\ \frac{\partial \mathbf{p}(\gamma, \eta)}{\partial (\gamma, \eta)} &= \begin{bmatrix} \cos(\gamma) e^{+j\eta} & j \sin(\gamma) e^{+j\eta} \\ -\sin(\gamma) & 0 \end{bmatrix} \end{aligned}$$

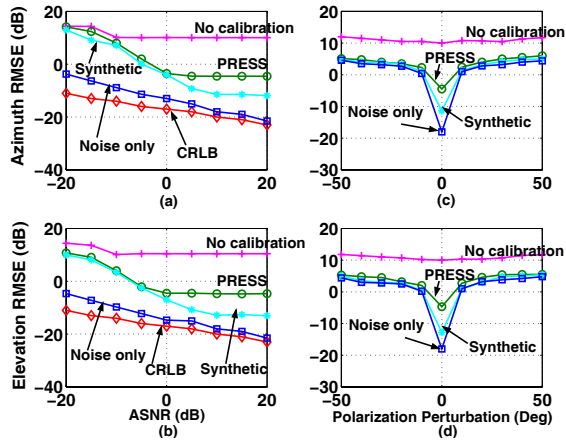


Fig. 3. (a) and (b): Azimuth and elevation RMSE dependence on ASNR with perfect polarization angle knowledge. **(c) and (d):** Azimuth and elevation RMSE dependence on polarization angle perturbation at ASNR = 10 dB.

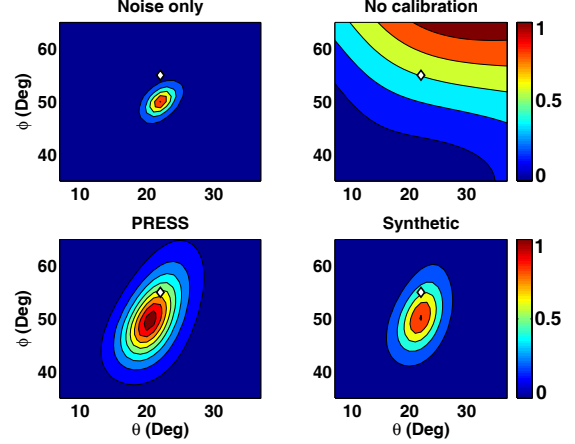


Fig. 4. Example Capon DF spectrum. The diamond in the figure indicates the true source location.

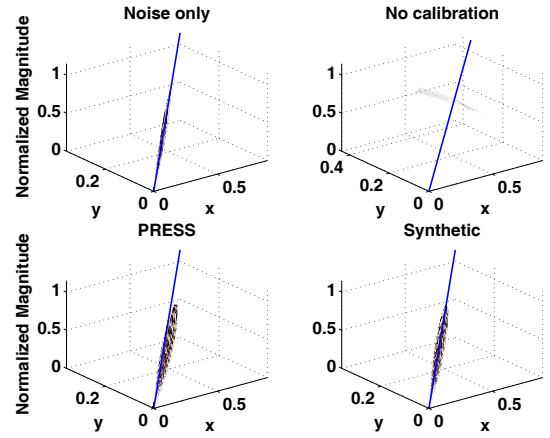


Fig. 5. Example Capon DF spectrum in spherical coordinates. The solid line indicates the true DOA.

6. REFERENCES

- [1] A. Nehorai and E. Paldi, "Vector-Sensor Array Processing for Electromagnetic Source Localization," *IEEE Trans. Sig. Proc.*, vol. 42, pp. 376-398, Feb. 1994.
- [2] K.T. Wong and M.D. Zoltowski, "Closed-form Direction Finding and Polarization Estimation With Arbitrarily Spaced Electromagnetic Vector-sensors at Unknown Locations," *IEEE Trans. Ant. & Prop.*, vol. 48, pp. 671 - 681, May 2000.
- [3] K. W. Forsythe, "Utilizing waveform features for adaptive beamforming and direction finding with narrowband signals," *The Lincoln Laboratory Journal*, vol. 10, num. 2, pp. 99-126, 1997.